Wave flume testing of an oscillating-body wave energy converter with a tuned inerter

Keita Sugiura[a], Ryoko Sawada[a], Yudai Nemoto[b], Ruriko Haraguchi[a],
Takehiko Asai[c]

[a]*Graduate School of Systems and Information Engineering, University of Tsukuba, Japan*
[b]*College of Engineering Systems, University of Tsukuba, Japan*
[c]*Faculty of Engineering, Information and Systems, University of Tsukuba, Japan*

Abstract

In this study, the effectiveness of an oscillating-body WEC with a tuned inerter (TI) proposed by the authors is shown through wave flume testing. The TI mechanism consisting of a tuning spring, a rotational inertial mass, and a viscous damping component is able to increase energy absorption capability by taking advantage of the resonance effect of the rotational mass. This mechanism has been recently introduced for civil structures subjected to external loadings such as earthquakes and winds to decay vibration response immediately. The authors applied this mechanism to oscillating-body WECs and showed that the proposed WEC increased the power generation performance and broadened the effective frequency range without increasing the mass of the buoy itself through numerical simulation studies. To verify the validity of the proposed WEC experimentally, a small-scale prototype of the proposed device is designed and wave flume testing is carried out with various regular wave inputs of different frequencies. The results show that the WEC with the properly adjusted TI mechanism demonstrates better power generation performance compared to the conventional WEC over a wide range of wave frequencies.

Keywords: Wave energy converter, Tuned inerter, Wave flume testing, Renewable energy, Energy harvesting

1. Introduction

The public interest in renewable energy has risen over the last decades. In this social situation, ocean wave energy has been considered to be one

of the promising renewable energy sources because of its tremendous energy potential [1] and many researchers have been devoting considerable effort to improve the power take-off (PTO) system from the ocean wave [2, 3, 4, 5, 6]. Generally, the PTO systems for wave energy converters (WECs) can be classified into three categories, i.e., oscillating water columns, oscillating bodies, and overtopping devices. Among these WECs, the oscillating-body type which consists of a floating buoy has been expected to be a promising strategy because of its availability in deep offshore regions and its extensibility by arraying many buoys.

It is well-known that the power generation efficacy of oscillating-body WECs is improved when the buoy is in resonance with the incoming wave. While, typically, the natural frequency of the buoy with reasonable size tends to be much higher than the frequencies of ocean waves [7]. Therefore, to take advantage of the full potential of oscillating-body WECs, the natural frequency of the buoy needs to be shifted closer to the ocean wave frequency. Toward that end, researchers and engineers have been trying to increase the mass of the buoy part, leading to the idea of a system of two objects consisting of a semi-submerged buoy and a lower submerged object which provides an additional inertia to the buoy part [8, 9, 10, 11, 12, 13]. This strategy has achieved certain results, however, the problem seems to lie in the fact that a huge additional mass needs to be submerged to adjust the natural frequency to the ocean wave frequency, which is not practical from the viewpoint of cost and workability.

To address this problem, the authors proposed the oscillating-body WEC with a tuned inerter (TI) [14]. The concept of the inerter was originally proposed by Smith [15] and the inerter generates force proportional to the relative acceleration by using gears or flywheels. Also, WECs with the inerter have been already proposed so far [16, 17, 18, 19, 20]. Based on the concept of inerter, the TI mechanism was proposed to protect civil structures subjected to external loadings such as earthquakes and strong winds [21]. In this mechanism, a rotational inertial mass which produces inerter is combined with a tuning spring and a viscous damping component. Due to the tuning spring, the inerter part is decoupled from the primary structure. Then, the tuning spring stiffness and the rotational inertial mass are designed so that the rotational inertial mass, not the mass of the primary structure, resonates with the external loading, leading to the improvement of the energy dissipation by the viscous damping component mounted in parallel with the rotational mass. Moreover, the advantage of the system is that

2

a significantly amplified mass effect can be achieved easily from a relatively small physical mass due to a ball screw mechanism. Originally, in this TI mechanism, fluid viscous dampers, which convert vibratory energy to heat, were supposed to be used. While, the authors utilized a motor as the viscous damping component, proposing the tuned inertial mass electromagnetic transducer (TIMET) [22, 23] to convert vibratory energy to electrical energy. So far, applications of this device not only to WECs but also to civil structures [24, 25] have been investigated and the effectiveness was shown through numerical simulation studies.

The main objective of the present study is experimental verification of the TI WEC proposed by the authors. In particular, a small-scale prototype of the device is designed and wave flume testing is carried out with various regular wave inputs of different frequencies. First, to explain the difference, the conventional oscillating-body WEC introduced in the literature and the TI WEC are described. Next, the analytical models are introduced and the equations of motion for both systems are developed. Then, the conditions of the wave flume testing are described and the obtained results are shown. In addition, numerical simulation studies are implemented to examine the validity of the developed models for the small-scale prototypes. Finally, conclusions gained from this study follow.

2. Mechanism

In this section, the mechanism for the proposed TI WEC is introduced by using the small-scale model used for the wave flume testing and its equation of motion is derived. For simplicity, the model is developed to restrict the motion to the heave direction only.

2.1. SDOF WEC

Firstly, the mechanism of the conventional WEC [26] is reviewed briefly. When only the heave direction is considered, the conventional WEC can be modeled as a single-degree-freedom (SDOF) system. Therefore, the conventional WEC is called a SDOF WEC hereafter in the article. As illustrated in Figure 1(a), the SDOF WEC considered here consists of a floating cylindrical buoy, a three-phase motor, and a constant-force spring. The cylindrical buoy whose diameter is D is interfaced with the motor through a tether which spools around a pulley of radius r_p keyed to the motor shaft. For practical reasons of conducting wave flume testing, the motor is installed above the
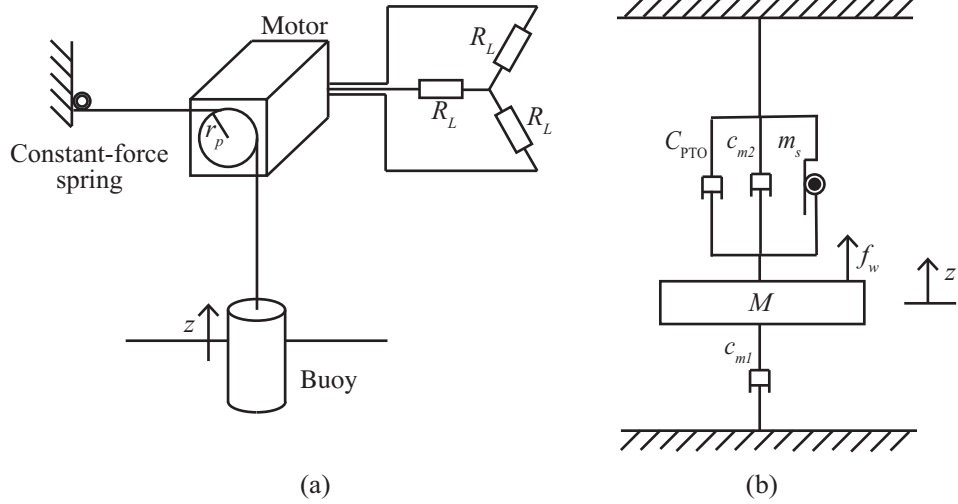
Figure 1: SDOF WEC: (a) Schematic illustration, (b) Model.

water in this research as shown in Figure 1(a). However, even when the buoy is connected through a tether from the bottom of the buoy to the motor submerged under water and anchored to the ocean floor as in [26], the equation of motion developed below still holds.

For practical reasons of conducting wave flume testing, the motor is installed above the water. However, the equation of motion developed below holds for when the motor is submerged and anchored to the ocean floor, allowing the device to be installed offshore. The constant-force spring, which exerts constant-force F_{cf} regardless of its deformation, is used to generate the tension of the tether to prevent the tether from sagging and slipping and to cancel part of the downward gravity force acted on the buoy. Therefore the magnitude of the constant-force spring affects the equilibrium position of the buoy, however, it does not contribute to the equation of motion and the conceptual model developed below for the case of cylinder-shaped buoy.

The SDOF WEC can be modeled as in Figure 1(b). Let z be the displacement of the buoy. The upward direction is taken as positive and the static equilibrium state is the origin. Then, the equation of motion of the buoy would be

$$(M + m_s)\ddot{z} + (c_{m1} + c_{m2} + C_{\text{PTO}})\dot{z} = f_w \tag{1}$$

where M is the mass of the buoy, m_s is the inertial mass including the motor and the pulley, C_{PTO} is the damping coefficient caused by the motor, and c_{m1}

4

and c_{m2} are the unavoidable mechanical dampings caused in the device. Even though the dampings c_{m1} and c_{m2} can be merged for the SDOF WEC model, these dampings are considered separately here because of the TI WEC model introduced next.

In addition, f_w is the hydrodynamic force, which is described by

$$f_w = f_a + f_b + f_c \tag{2}$$

where f_a is the excitation force, f_b is the hydrostatic force due to buoyancy, and f_c is the radiation force. Let the Fourier transforms of f_a and f_c be denoted $\hat{f}_a$ and $\hat{f}_c$, respectively. The relation between the excitation force f_a and the amplitude of the incident wave a is given in the frequency domain using a transfer function $F_a(\omega)$ as

$$\hat{f}_a(\omega) = F_a(\omega)\hat{a}(\omega) \tag{3}$$

where $\hat{a}(\omega)$ is the Fourier transform of a. The hydrostatic force becomes a linear function of z expressed as

$$f_b = -K_w z \tag{4}$$

where K_w is given with the gravity acceleration g and water density ρ by

$$K_w = \rho g \pi \left(\frac{D}{2}\right)^2 \tag{5}$$

and the radiation force f_c is given as

$$\hat{f}_c(\omega) = -(j\omega m_a(\omega) + c_r(\omega))\hat{\dot{z}} \tag{6}$$

where $m_a(\omega)$ and $c_r(\omega)$ are the added mass and the radiation damping, respectively and are frequency dependent. Note that j is the imaginary unit satisfying $j^2 = -1$.

2.2. WEC with tuned inerter

Next, the mechanism of the proposed TI WEC illustrated in Figure 2(a) is introduced. In addition to the components of the SDOF WEC, the TI WEC has the tuning spring installed between the buoy and the pulley and the intentionally large rotational inertial mass added to the motor shaft. Let
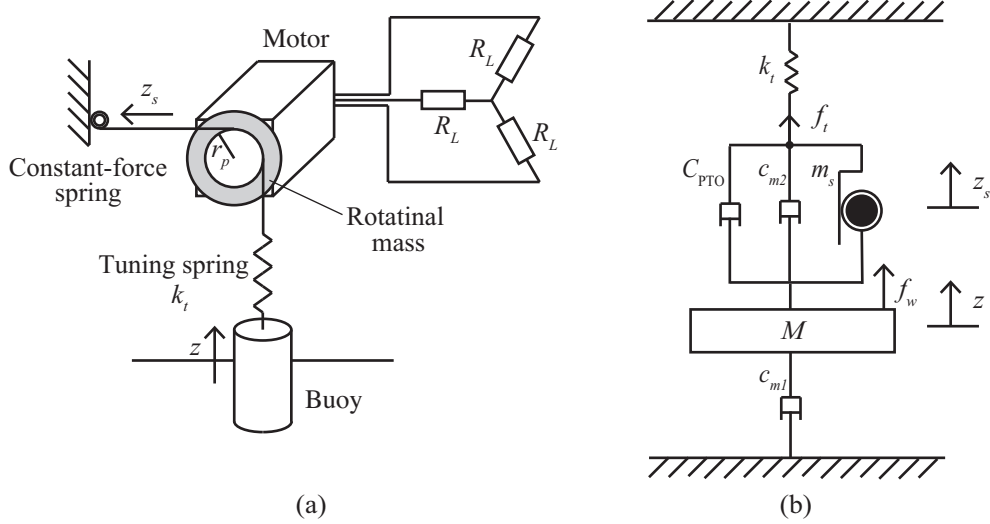
Figure 2: WEC with TI: (a) Schematic illustration, (b) Model.

f_t be the tuning spring force, then the equation of motion of the buoy for the proposed WEC can be written as

$$M\ddot{z} + c_{m1}\dot{z} = f_w - f_t \qquad (7)$$

where f_w is the hydrodynamic force given by Eq. (2). Let z_s be the displacement of the rotational inertial mass, then in the TI mechanism, the equation of the equilibrium given by

$$m_s\ddot{z}_s + (c_{m2} + C_{\text{PTO}})\dot{z}_s = f_t \qquad (8)$$

must hold. Because the deformation of the tuning spring becomes $z - z_s$, the tuning spring force f_t can be expressed with the tuning spring stiffness k_t by

$$f_t = k_t(z - z_s) \qquad (9)$$

Therefore, the proposed WEC with the TI becomes a two-degree-of-freedom (2DOF) system and the power generation by the motor can be improved by designing the tuning spring stiffness and the rotational mass appropriately based on the frequency of the external wave input [14].

2.3. Power

Finally, the damping coefficient and the power generated by the three-phase motor is defined here. As shown in Figs. 1(a) and 2(a), we assume

6

that the motor used here is a three-phase motor which is connected to three resistive loads of resistance R_L in star configuration. Let R and K_e be the internal or coil resistance and the back-EMF constant of the motor, respectively, then the damping coefficient by the motor can be approximated as

$$C_{\mathrm{PTO}} = \frac{3K_e^2}{2r_p^2(R + R_L)} \tag{10}$$

The detailed derivation can be found in [27].

And in this research, the generated power P_g is defined by the summation of the dissipated power by the three resistive loads, i.e.,

$$P_g(t) = \frac{v_a^2 + v_b^2 + v_c^2}{R_L} \tag{11}$$

where v_a, v_b, and v_c are the voltages across the resistive loads. Thus the average power from time 0 to t_f is defined as

$$\bar{P}_g = \frac{1}{t_f} \int_0^{t_f} P_g(t)dt \tag{12}$$

3. Wave flume testing

Wave flume testing is carried out to evaluate the power generation performance of the proposed WEC in this section. First, the experimental setup is introduced. Next, two preliminary tests are implemented to estimate the parameter values for the mechanical damping coefficients c_{m1} and c_{m2} and the optimal resistive loads R_L for the small-scale models developed for this research. Then, the results obtained from the wave flume testing are shown.

3.1. Experimental setup

To validate the effectiveness of the proposed TI WEC, laboratory experiments of a 1:36 scale model are carried out in the wave flume located at the Center for Research in Isotopes and Environmental Dynamics (CRiED), University of Tsukuba, Japan. The wave flume is 21 m long, 0.5 m wide and 0.5 m deep and the water depth is 0.3 m. The WEC prototype device is placed at a distance 6 m from the wave generator. In addition, a wave gauge is mounted 0.5 m ahead of the device in the direction of propagation. The experimental setup is shown in Figure 3.
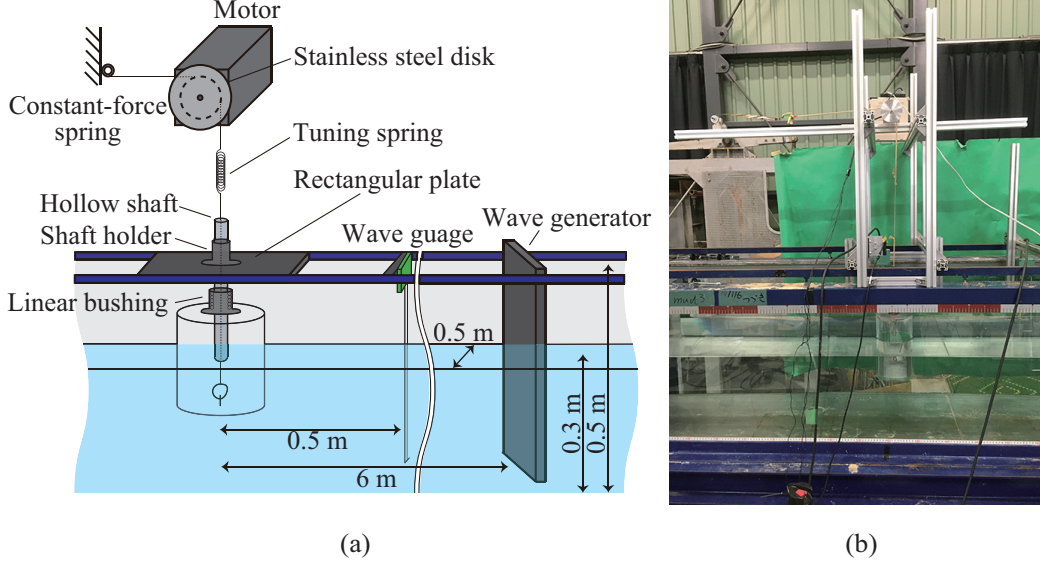
Figure 3: Experimental setup: (a) Schematic illustration, (b) Photograph.

The photograph of the small-scale buoy developed for this research is shown in Figure 4(a). A vertical cylinder used as the floating body has a diameter of 140 mm and a height of 220 mm. The buoy draft is set to 136 mm and a constant-force spring whose output force is 0.98 N is employed, thus some glass sand is added in the cylinder so that the mass including a linear bushing becomes 2.1 kg. The linear bushing is inserted in the coaxial bore of the cylinder to restrict the buoy motion to the heave direction along a hollow shaft of diameter 13 mm. The hollow shaft is erected on a horizontal rectangular plate fixed to the structure of the wave flume using a shaft holder as illustrated schematically in Figure 3(a). Thus the hollow shaft does not vibrate during the tests. As explained in the previous section, the cylinder is mechanically coupled with the motor through the tether, which goes through the hollow shaft from the bottom of the cylinder and spools around the pulley keyed to the motor shaft. A three-phase permanent-magnet synchronous motor used in the prototype is a YASKAWA SGMMV-A1A [28]. The back-EMF constant of the motor stated on the product specification is 0.0516 Nm/Arm, which has been transformed for practical convenience by $\frac{0.0516}{\sqrt{1.5}\sqrt{3}} = 0.0243$ V/rad/sec. Also, the constant-force spring which is employed to prevent the tether from sagging is installed at the other end of the tether. The parameters used in the experiment appear in Table 1. It should
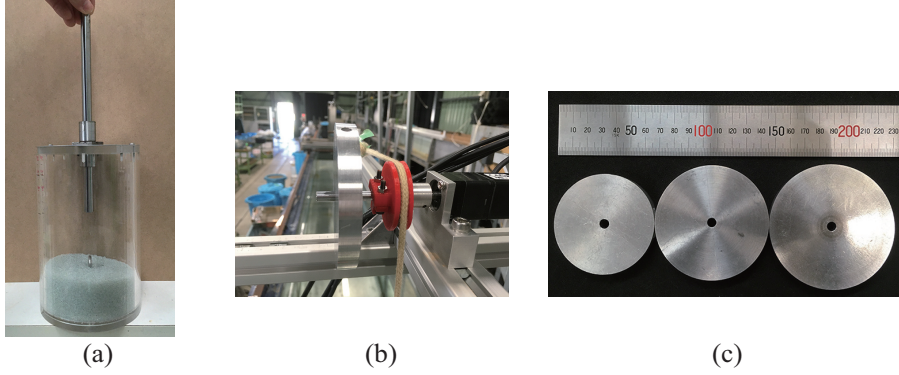
Figure 4: Photographs: (a) Buoy, (b) Motor part, (c) Stainless steel disks.

Table 1: Parameter values used for the wave flume testing

	Parameters	Values
Buoy mass	M	2.1 kg
Buoy diameter	D	140 mm
Buoy height	H	220 mm
Buoy draft	L	136 mm
Constant-force spring	F_{cf}	0.98 N
Mechanical damping	c_{m1}	2.35 Ns/m
Mechanical damping	c_{m2}	0.45 Ns/m
Back-EMF constant	K_e	0.0243 V/rad/s
Internal or coil resistance	R	5.25 Ω
Water density	ρ	1000 kg/m^3

be noted that for the small-scale model of 1:36, the diameter of 140 mm and the mass of 2.1 kg corresponds to 5.04 m and 98.0 t for a full-scale WEC from the Froude scaling laws based on the assumption that the most dominating phenomena of the model test is governed by potential flow [29].

Figure 4(b) and (c) are the photographs of the motor part and the stainless steel disks to add rotational inertial mass for the TI WEC. The pulley is made by a 3D printer and its radius r_p is 18 mm. A tuning spring whose stiffness 10 N/m is installed between the cylinder and the pulley for the TI

Table 2: Experimental types and parameters

Type	Mechanism	r_p (mm)	k_t (N/m)	m_s (g)	R_L (Ω)
A-R1	SDOF	18	N/A	5.3	5
A-R2	SDOF	18	N/A	5.3	13
B1-R1	TI	18	10	156.3	5
B1-R2	TI	18	10	156.3	13
B2-R1	TI	18	10	283.3	5
B2-R2	TI	18	10	283.3	13
B3-R1	TI	18	10	386.3	5
B3-R2	TI	18	10	386.3	13

WEC. The rotational inertial mass m_s is defined as

$$m_s = \frac{I}{r_p^2} \tag{13}$$

where I is the moment of inertia including the stainless steel disk, the motor, and the shaft. Thus, even the SDOF WEC without the stainless steel disk has a small inertial mass of 5.3 g. While, for the TI WEC, the inertial mass is increased to 156.3 g, 283.3 g, and 386.3 g by adding the stainless steel disks. These three inertial masses are employed to conduct a comparative study and investigate how the effective frequency range is changed. Hereafter, in this article, the SDOF WEC is denoted by Type A and the TI WECs are denoted by Type B1, B2, and B3 depending on the inertial mss values as summarized in Table 2.

3.2. Preliminary tests

The power generation performance is highly dependent on the resistive loads R_L which are difficult to predict due to the existence of the energy loss caused in the devices. Thus, the mechanical damping coefficients c_{m1} and c_{m2} in the models and the optimal resistive loads R_L for the devices in Figs. 1 and 2 are determined experimentally here.

3.2.1. Decay tests

The mechanical damping coefficients c_{m1} and c_{m2} existed in the developed devices are estimated for accurate modeling first. For simplicity, in this research, these mechanical damping coefficients are assumed to be constant
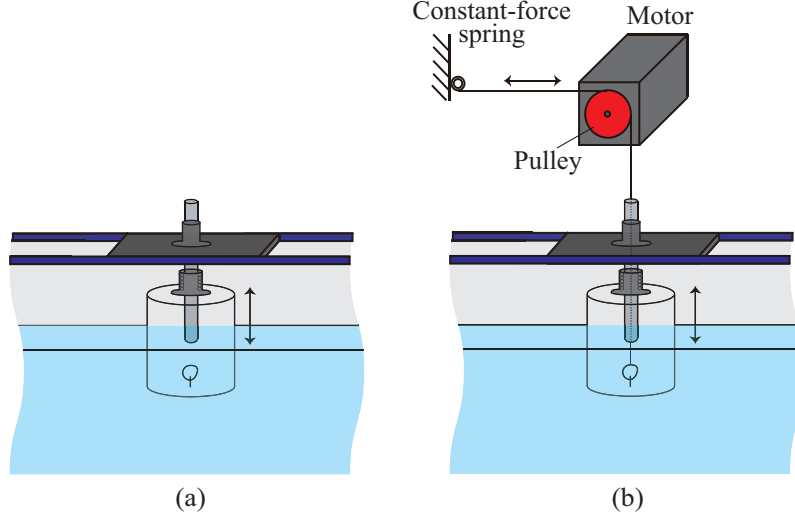
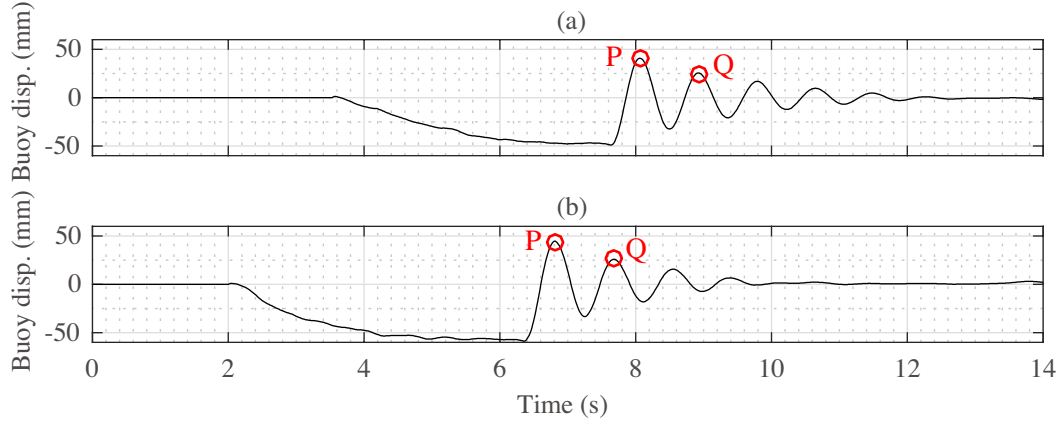Figure 5: Decay test setup: (a) Buoy with the linear bushing, (b) SDOF WEC.

Figure 6: Decay test results: (a) Buoy with the linear bushing, (b) SDOF WEC.

regardless of the vibration frequency and the values are determined based on the free vibration decay test under still water as follows. We assume that the SDOF and the TI WECs have the same mechanical damping coefficients. We also assume that c_{m1} comes from the friction between the linear bushing and the hollow shaft and that c_{m2} is attributed mainly to the motor and the constant-force spring. Thus, to obtain c_{m1} and c_{m2}, two decay tests are carried out on the conditions illustrated in Figure 5.

11

For the first decay test, the buoy is disconnected from the motor as shown in Figure 5(a). Then the buoy with the linear bushing is submerged manually and released gently. The dynamical displacement of the buoy recorded by a laser displacement sensor is shown in Figure 6(a).

From the logarithmic decrement method [30], the damping factor ζ is given with the data of points P and Q in Figure 6(a) by

$$\zeta = \frac{1}{2\pi} \ln \frac{u_P}{u_Q} \tag{14}$$

where u_P is the amplitude at the beginning of a cycle and u_Q is the amplitude at the end of the cycle. In the first decay test, the recorded values for u_P and u_Q are 40.9 mm and 25.5 mm, respectively, then, from Eq. (14), ζ is calculated to be 0.075. Also, the damped natural frequency ω_d is given by

$$\omega_d = \frac{2\pi}{t_Q - t_P} \tag{15}$$

where t_P is the time at the beginning of the cycle and t_Q is the time at the end of the cycle. The values measured in the test are $t_P = 8.06$ s and $t_Q = 8.92$ s, thus the damped natural frequency ω_d becomes 7.31 rad/s from Eq. (15). The equation of motion of the buoy for the first decay test considering the hydrodynamic force at $\omega = \omega_d = 7.31$ rad/s becomes

$$(M + m_a(\omega_d))\ddot{z} + (c_{m1} + c_r(\omega_d))\dot{z} + K_w z = 0 \tag{16}$$

Thus, the summation of the damping coefficients including the radiation damping $c_r(\omega_d)$ can be expressed as

$$c_{m1} + c_r(\omega_d) = 2\zeta\sqrt{K_w(M + m_a(\omega_d))} \tag{17}$$

where the values for $c_r(\omega_d)$ and $m_a(\omega_d)$ are provided as 0.71 Ns/m and 0.64 kg, respectively, by the software WAMIT [31]. In this way, the mechanical damping c_{m1} is estimated as 2.35 Ns/m. Note that the values for $m_a(\omega_d)$ obtained from the approximated relationship about the damped natural frequency

$$\omega_d^2 \approx \frac{K_w}{M + m_a(\omega_d)} \tag{18}$$

is 0.73 kg, which is relatively close to the values calculated by the WAMIT.

To estimate the value for c_{m2}, the second decay test is conducted in the same way as the first one. The buoy shown in Figure 5(b) which is the setup for the SDOF WEC is used. In the second decay test, $u_P = 40.8$ mm, $u_Q = 26.0$ mm are measured, leading to $\zeta = 0.086$ by Eq. (14). Also, $\omega_d = 7.22$ rad/s is obtained with $t_P = 6.81$ s, $t_Q = 7.68$ s by Eq. (15). The values for $c_r(\omega_d)$ and $m_a(\omega_d)$ provided by the WAMIT at $\omega = \omega_d = 7.22$ rad/s are 0.72 Ns/m and 0.64 kg, respectively. Thus considering the equation of motion for the SDOF WEC given by Eq. (1), the relationship

$$c_{m1} + c_{m2} + c_r(\omega_d) = 2\zeta\sqrt{K_w(M + m_s + m_a(\omega_d))} \qquad (19)$$

holds. Considering $m_s = 5.3$ g for the model of the SDOF WEC, we have $c_{m2} = 0.45$ Ns/m. Also, $m_a(\omega_d)$ calculated from Eq. (18) is 0.80 kg, which is somewhat different from the value calculated by the WAMIT. This discrepancy seems be attributable to the fact that the experimental setup does not satisfy the conditions assumed in the WAMIT, which will be discussed particularly in 4.2.

3.2.2. Optimal resistive load test

The optimal resistive loads R_L for the power generation of the SDOF WEC and the TI WEC are sought experimentally as well. Regular wave of 1.0 s period is input to the SDOF WEC and the TI WEC with $m_s = 156.3$ g. These conditions correspond to Type A and Type B2 in Table 2. To find the resistive loads which maximize power generation, the resistive loads connected to the motor are changed from 4 Ω to 15 Ω with 1 Ω increment.

The average power generated by the different resistive loads are compared in Figure 7. As can be seen, the average power of Type A peaks when $R_L = 5$ Ω, while Type B2 maximizes its power generation when $R_L = 13$ Ω. So these results clearly show that the optimal resistive load depends on the conditions of WECs. However, finding the optimal resistive load for Type B1 and B3 or under regular waves of different periods makes this comparative study more complex. Besides, the objective of this article is to show the mechanical advantage of the TI WEC experimentally. Therefore, the power generation with the resistive loads of 5 Ω and 13 Ω are investigated for Type A, B1, B2 and B3 in the wave flume testing in this article. It should be noted that $C_{\mathrm{PTO}} = 0.27$ Ns/m when $R_L = 5$ Ω and $C_{\mathrm{PTO}} = 0.15$ Ns/m when $R_L = 13$ Ω from Eq. (10).
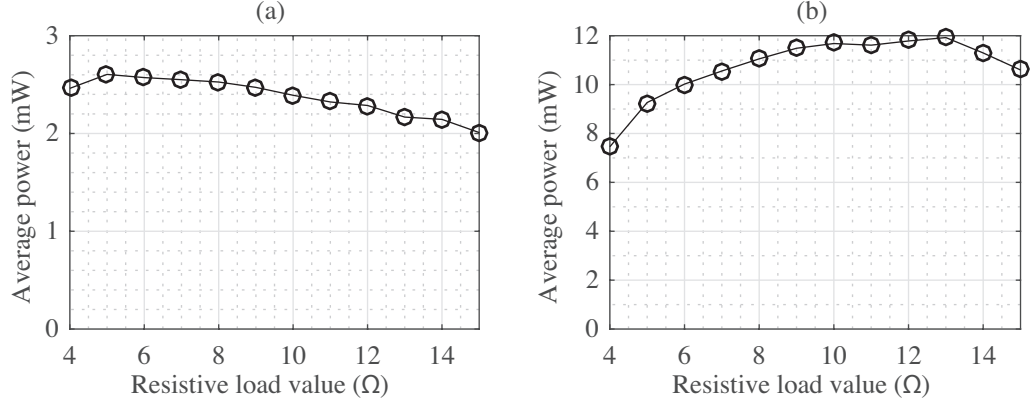
13

Figure 7: Average power generation vs. resistive load value: (a) SDOF WEC (Type A), (b) TI WEC (Type B2).

3.3. Results

Finally, the wave flume testing is conducted. Six kinds of regular waves of different dominant periods $T_p = 0.8$ s, 0.9 s, 1.0 s, 1.1 s, 1.2 s, and 1.3 s produced by the wave generator are input to the eight types of WECs summarized in Table 2. The time histories of the wave elevation of the six time periods are shown in Figure 8. The waves shown in Figure 8 are measured by the wave gauge during the tests for Type A. The wave generator is controlled so that the wave elevations become 40 mm, however, some variations are observed depending on the wave period due to the difficulty of controlling the wave generator. Note that from the Froude scaling laws, the investigated wave period range of 0.8 - 1.3 s and wave elevation of 40 mm corresponds to 4.8 - 7.8 s and 1.44 m for a full-scale WEC.

The measured average power generations are summarized in Table 3. These values are calculated by Eqs. (11) and (12) using the data for a duration of 100 s after the dynamics of the buoy reaches the steady state. Bar graphs are used to compare the experimental average power in Figure 9, in which the average values obtained from the numerical simulation by the developed models in the next section are indicated by circles and crosses as well. The experimental results clearly show that the proposed TI WEC improves the power generation performance of the SDOF WEC significantly. In addition, it is evident from the performances of Type B1, B2, and B3 that the TI WEC is able to change the effective period range depending on its rotational inertial mass value. More precisely, the SDOF WEC is unable
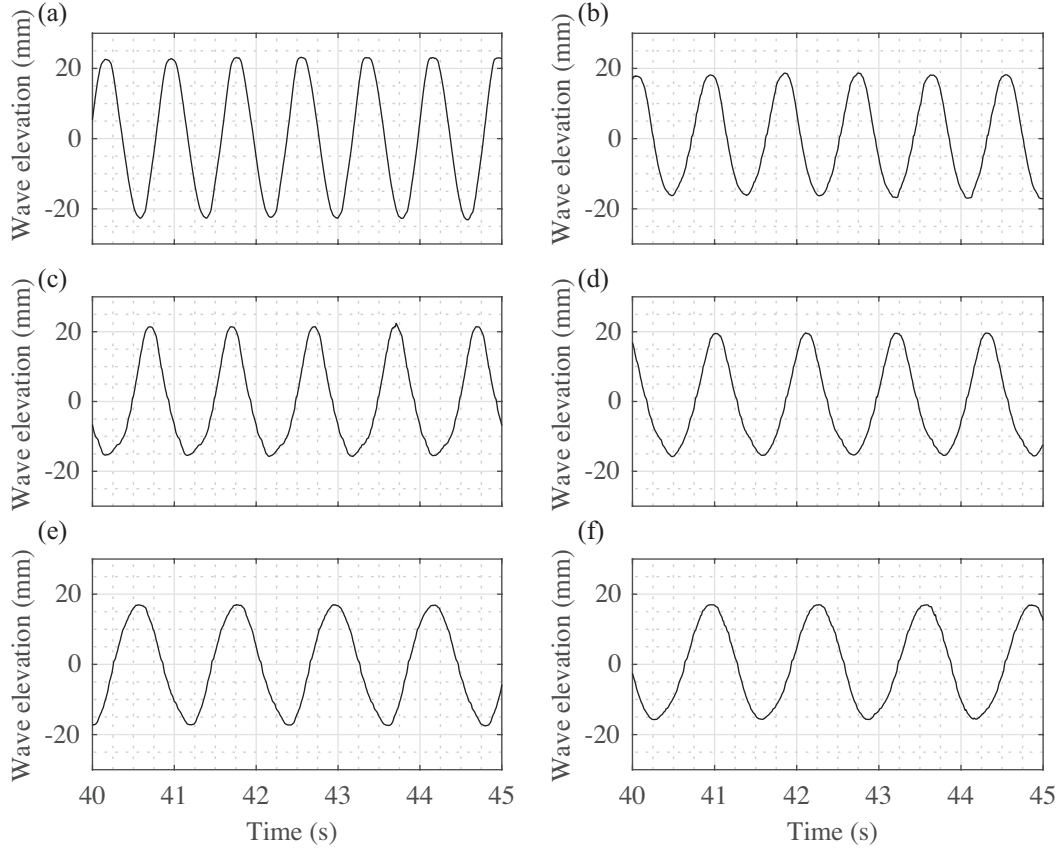
14
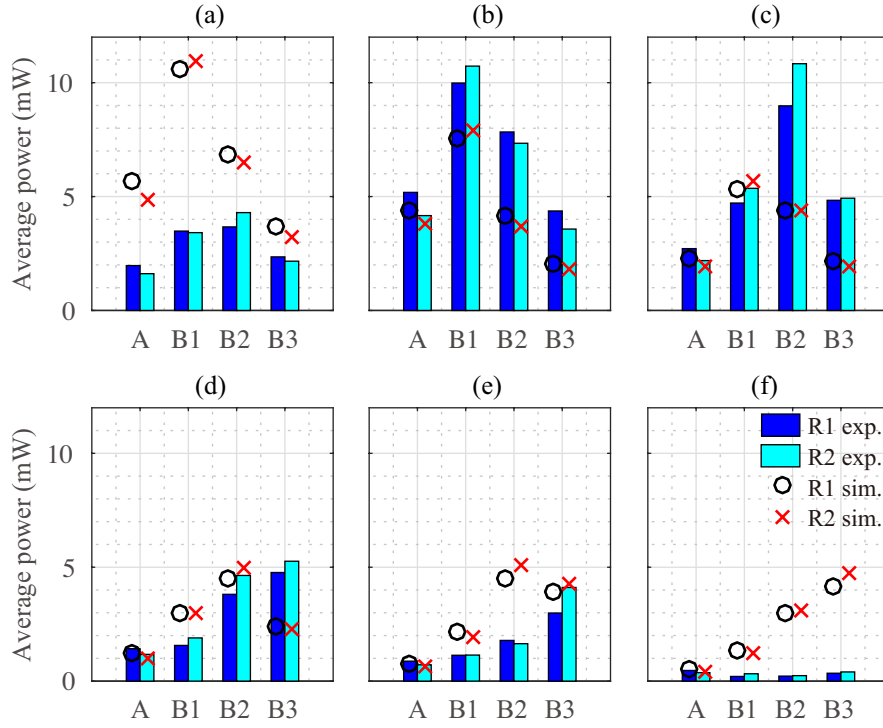
Figure 8: Wave elevation: (a) $T_p = 0.8$ s, (b) $T_p = 0.9$ s, (c) $T_p = 1.0$ s, (d) $T_p = 1.1$ s, (e) $T_p = 1.2$ s, (f) $T_p = 1.3$ s,.

to adjust to long-period waves, however, the TI WEC with larger rotational inertial mass works better in the long-period band without increasing the mass of the buoy itself. Also, the results confirm that the SDOF WEC performs better with resistive loads of 5 Ω than with resistive loads of 13 Ω. While, as expected, it is observed that the optimum resistive loads for the TI WEC vary according to the rotational inertial mass value and the input wave period.

4. Numerical simulation

Numerical simulation studies are conducted using the parameter values introduced in the previous section to compare with the test results and to

Table 3: Generated average power (mW)

Type	Input wave period (T_p)					
	0.8 s	0.9 s	1.0 s	1.1 s	1.2 s	1.3 s
A-R1	1.97	5.18	2.71	1.42	0.88	0.47
A-R2	1.62	4.16	2.19	1.17	0.72	0.37
B1-R1	3.48	9.98	4.72	1.57	1.14	0.21
B1-R2	3.42	10.73	5.36	1.90	1.14	0.32
B2-R1	3.67	7.84	8.98	3.81	1.79	0.22
B2-R2	4.30	7.34	10.83	4.64	1.64	0.24
B3-R1	2.35	4.37	4.84	4.77	2.99	0.35
B3-R2	2.16	3.57	4.93	5.26	4.11	0.40

Figure 9: Comparisons of generated average power: (a) $T_p = 0.8$ s, (b) $T_p = 0.9$ s, (c) $T_p = 1.0$ s, (d) $T_p = 1.1$ s, (e) $T_p = 1.2$ s, (f) $T_p = 1.3$ s,.
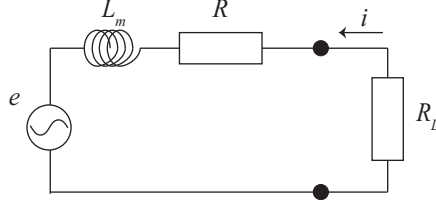
Figure 10: Approximate circuitry.

discuss the validity of the developed models here.

4.1. Problem formulation

First, the power generated in the wave flume testing is simulated using the models developed in the previous section by the method proposed in [14]. In this reference, a DC motor is assumed for generating power, so the three-phase motor employed in the prototype is approximated by the technique introduced in [27, 32] as the circuit shown in Figure 10. And, as stated before, the excitation force $F_a(\omega)$, added mass $m_a(\omega)$, and radiation damping $c_r(\omega)$ are given by the software WAMIT in this research, then the equations of motion given by Eq. (1) for the SDOF WEC and Eqs. (7) and (8) for the TI WEC are approximated in a state-space form of finite dimensional linear time invariant system by the system identification technique as

$$\dot{\mathbf{x}} = \mathbf{A}\mathbf{x} + \mathbf{B}a \qquad (20)$$

$$e = \mathbf{C}\mathbf{x} \qquad (21)$$

where $\mathbf{x}$ is the state vector, e is the voltage generated by the DC motor, and $\mathbf{A}$, $\mathbf{B}$, and $\mathbf{C}$ are appropriate matrices. The wave amplitude a is taken to be the wave amplitude measured by the wave gauge placed 0.5 m ahead of the buoy for the approximation of an accurate causal system.

Considering the circuit shown in Figure 10 , and assuming that the effect of the inductance L_m can be ignored, the input current to the motor would be

$$i = -\frac{e}{R + R_L} = -\frac{\mathbf{C}\mathbf{x}}{R + R_L} \qquad (22)$$

Also, on the assumption of use of a DC motor, the generated power can be defined as

$$P_g(t) = -ie - Ri^2 \qquad (23)$$

17

where the second term denotes the energy loss due to the internal or coil resistance of the motor [26]. Thus, once the state-space representation given by Eqs. (20) and (21) are derived, the power generation can be evaluated by Eq. (23). The details of this derivation are not described in this paper. However, the outline of the method can be found in [14].

Additionally, to investigate the dependence of the power generation performance on the input wave frequency ω, sinusoidal waves emulating the regular waves measured in the wave flume testing, which is given by

$$a(t) = a_0 \sin \omega t \tag{24}$$

are input into the system expressed by Eqs. (20) and (21) as well. a_0 is the amplitude of the sinusoidal wave, thus the wave elevation of the sinusoidal wave is considered to be $2a_0$. Let the transfer function of this system be $G(s)$, which is defined as

$$G(s) = \mathbf{C}(s\mathbf{I} - A)^{-1}\mathbf{B} \tag{25}$$

where s denotes the Laplace transform variable. Then, the voltage $e(t)$ and the current $i(t)$ are given by

$$e(t) = a_0|G(j\omega)| \sin(\omega t - \angle G(j\omega)) \tag{26}$$

$$i(t) = -\frac{a_0|G(j\omega)|}{R + R_L} \sin(\omega t - \angle G(j\omega)) \tag{27}$$

Substituting Eqs. (26) and (27) into Eq. (23) yields

$$P_g(t) = \frac{R_L a_0^2 |G(j\omega)|^2}{(R + R_L)^2} \sin^2(\omega t - \angle G(j\omega)) \tag{28}$$

The average power generation for 1 cycle, i.e., from 0 to $\frac{2\pi}{\omega}$, can be calculated by

$$\bar{P}_g = \frac{R_L a_0^2 |G(j\omega)|^2}{(R + R_L)^2} \frac{\omega}{2\pi} \int_0^{2\pi/\omega} \sin^2(\omega t - \angle G(j\omega)) dt \tag{29}$$

The integration part in the above equation reduces to $\frac{\pi}{\omega}$, thus, the average power generation under the sinusoidal waves given by Eq. (24) becomes

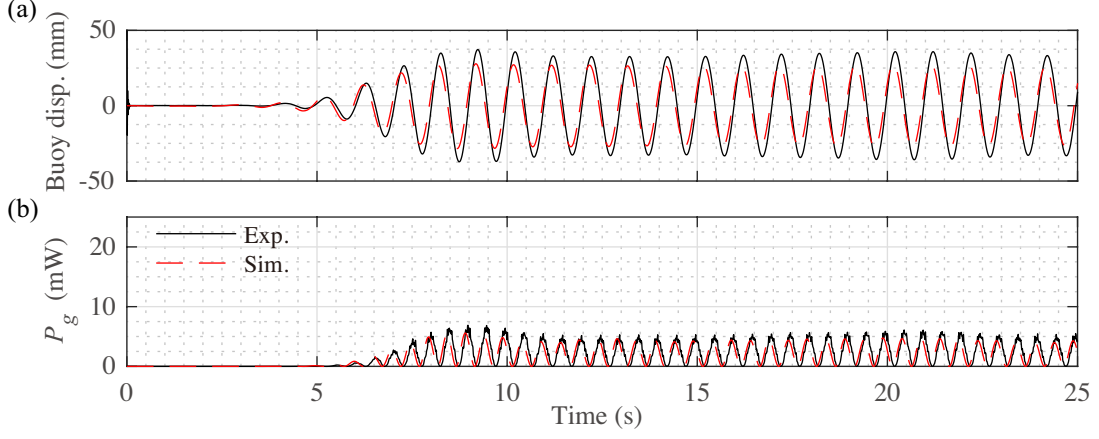$$\bar{P}_g = \frac{R_L a_0^2 |G(j\omega)|^2}{2(R + R_L)^2} \tag{30}$$

18

Figure 11: Comparisons of time histories of the experimental and simulation results for Type A-R1: (a) Buoy displacement, (b) Power generation.

4.2. Results

The results obtained from the numerical simulation are compared with those from the experiments and the reliability of the developed models are examined. Figures 11 and 12 show the time histories of the generated power and the displacement of the buoy for A-R1 and B2-R2 cases under the regular wave of $T_p = 1.0$ s. Also, the average power generations of all cases calculated from numerical simulations are marked by circles for R1 cases ($R_L = 5 \ \Omega$) and crosses for R2 cases ($R_L = 13 \ \Omega$) in Figure 9 to compare the experimental results shown by bar. Unfortunately, considerable discrepancies are observed especially in the TI WEC, i.e., Type B1, B2, and B3 and these results imply the difficulty of developing accurate analytical models of the 2DOF small-scale prototype under external loadings of various frequencies. The possible causes of these discrepancies are that (1) the conditions for Airy linear wave or Stokes first-order theory assumed in the WAMIT [31, 33] are not satisfied in the wave flume testing [34]; (2) the drag force which might not be negligible around the natural frequency of the buoy, i.e., 0.8 s or 0.9 s, is ignored in the simulation [35]; (3) all the mechanical energy losses including the friction losses in the prototype and the nonlinear hysteresis damping by the constant-force spring are modeled by constant viscous damping coefficients [35]; and (4) waves reflected from side walls which act on the buoy are not considered in the simulation studies. However, these are common problems seen in experiments using small-scale models, which are difficult to address.
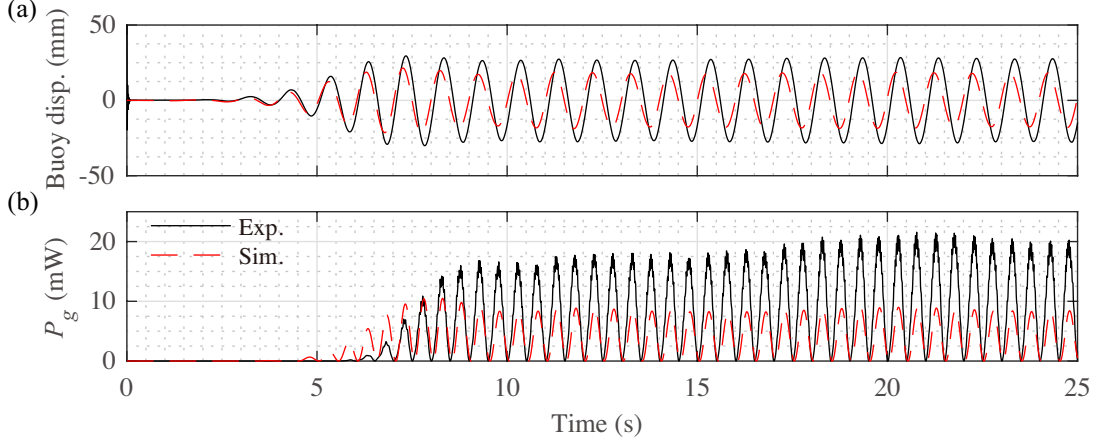
19

(a)

(b)

Figure 12: Comparisons of time histories of the experimental and simulation results for Type B2-R2: (a) Buoy displacement, (b) Power generation.

The average power generated from the sinusoidal waves using Eq. (30) are shown in Figure 13. The amplitude of the sinusoidal waves is set to 20 mm, corresponding to 40 mm wave elevation. In this figure, solid and dotted lines are used for the cases of R1 ($R_L = 5\ \Omega$) and R2 ($R_L = 13\ \Omega$), respectively. Note that the frequency ω of the sinusoidal waves are converted to the period T_p by the relationship $\omega T_p = 2\pi$ in Figure 13.

The results indicate that the effective frequency range of the TI WEC is broader than the conventional WEC. Also, it can be seen how the effective period range changes depending on the rotational inertial mass value m_s. In other words, the TI WEC is able to shift the effective period range to the higher period range without increasing the buoy mass M. And it can be observed that the resistive loads generating more power depends on the period of the input wave for the TI WEC cases, i.e., Type B1, B2, and B3. These trends agree with the experimental results shown in Figure 9, some differences are found in the time period range though. In addition, this figure shows how the average power of the proposed device is improved with respect to each input wave period.

5. Conclusions

This article reported the wave flume testing using the small-scale model of the WEC with the TI mechanism proposed by the authors and showed
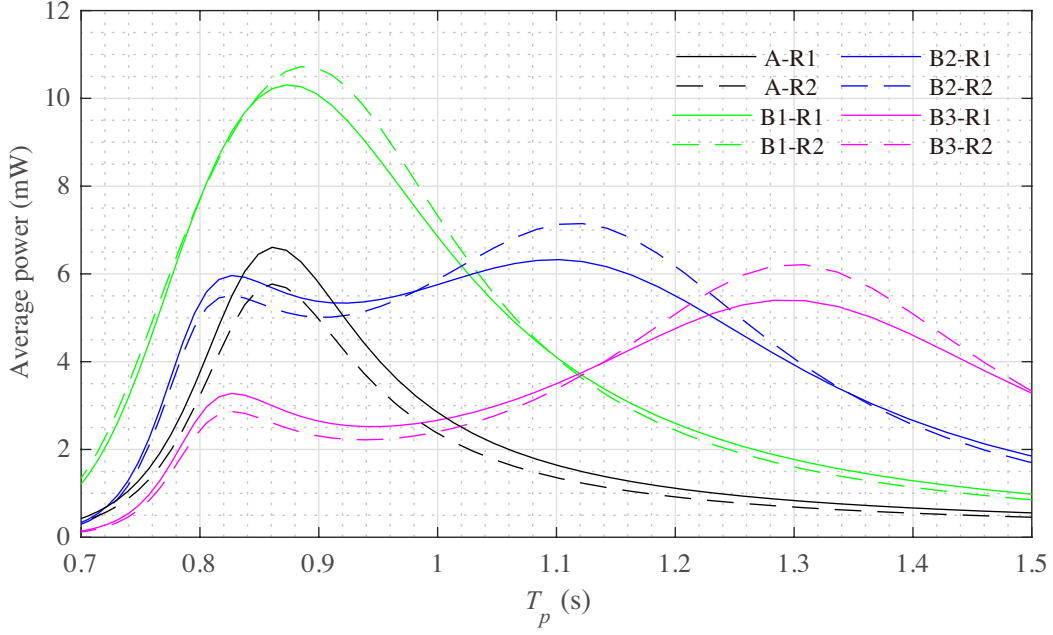
Figure 13: Average power under sinusoidal waves of 20 mm amplitude.

that the mechanism is able to improve the power generation performance of the conventional SDOF WEC significantly without increasing the buoy mass. Moreover, the results indicated that the effective frequency range of the TI WEC is adjustable by just changing the rotational inertial mass value. Also, to estimate the power generation performance, the models of the devices were established using the experimental data. However, developing accurate models including the energy loss of the small-scale prototypes was difficult and developed models were not adaptable enough for wide frequency range, which confirmed the importance of the experimental study.

For future work, experiments utilizing a full-scale model should be carried out in the ocean. In addition, a reliable analytical model to estimate the power generation more accurately should be developed and computational fluid dynamics (CFD) analysis is considered of value to improve numerical simulation study. And developing the mechanism to change the rotational inertial mass value simply is desired. Furthermore, algorithms for the feedback control technology to optimize not only the resistive loads but also the rotational inertial mass value in response to changing wave frequency should be proposed because the results obtained in this article demonstrate great

21

potential in a variable rotational inertial mass system to improve the power generation efficacy of oscillating-body WECs.

Acknowledgement

References

[1] M. Leijon, H. Bernhoff, M. Berg, O. Ågren, Economical considerations of renewable electric energy production—especially development of wave energy, Renewable Energy 28 (8) (2003) 1201 – 1209. doi:https://doi.org/10.1016/S0960-1481(02)00157-X.

[2] M. McCormick, Ocean Wave Energy Conversion, Dover Civil and Mechanical Engineering Series, Dover Publications, 2007.

[3] J. Scruggs, P. Jacob, Harvesting ocean wave energy, Science 323 (5918) (2009) 1176–1178. doi:10.1126/science.1168245.

[4] E. Rusu, F. Onea, A review of the technologies for wave energy extraction, Clean Energy 2 (1) (2018) 10–19. doi:10.1093/ce/zky003.

[5] B. Drew, A. R. Plummer, M. N. Sahinkaya, A review of wave energy converter technology, Proceedings of the Institution of Mechanical Engineers, Part A: Journal of Power and Energy 223 (8) (2009) 887–902. doi:10.1243/09576509JPE782.

[6] E. Ozkop, I. H. Altas, Control, power and electrical components in wave energy conversion systems: A review of the technologies, Renewable and Sustainable Energy Reviews 67 (2017) 106 – 115. doi:https://doi.org/10.1016/j.rser.2016.09.012.

[7] M. Eriksson, J. Isberg, M. Leijon, Hydrodynamic modelling of a direct drive wave energy converter, International Journal of Engineering Science 43 (17) (2005) 1377 – 1387. doi:https://doi.org/10.1016/j.ijengsci.2005.05.014.

[8] M. Vantorre, R. Banasiak, R. Verhoeven, Modelling of hydraulic performance and wave energy extraction by a point absorber in heave, Applied Ocean Research 26 (1) (2004) 61 – 72. doi:https://doi.org/10.1016/j.apor.2004.08.002.

[9] D. Evans, A. de O. Falcao, Hydrodynamics of ocean wave-energy utilization.

[10] J. Engström, M. Eriksson, J. Isberg, M. Leijon, Wave energy converter with enhanced amplitude response at frequencies coinciding with swedish west coast sea states by use of a supplementary submerged body, Journal of Applied Physics 106 (6) (2009) 064512. doi:10.1063/1.3233656.

[11] J. Engström, V. Kurupath, J. Isberg, M. Leijon, A resonant two body system for a point absorbing wave energy converter with direct-driven linear generator, Journal of Applied Physics 110 (12) (2011) 124904. doi:10.1063/1.3664855.

[12] V. Piscopo, G. Benassai, R. Della Morte, A. Scamardella, Cost-based design and selection of point absorber devices for the mediterranean sea, Energies 11 (4). doi:10.3390/en11040946.

[13] S. Bozzi, A. M. Miquel, A. Antonini, G. Passoni, R. Archetti, Modeling of a point absorber for energy conversion in italian seas, Energies 6 (6) (2013) 3033–3051. doi:10.3390/en6063033.

[14] R. Haraguchi, T. Asai, Enhanced power absorption of a point absorber wave energy converter using a tuned inertial mass, Energy (Under review). doi:10.31224/osf.io/q9k5h.

[15] M. C. Smith, Synthesis of mechanical networks: the inerter, IEEE Transactions on Automatic Control 47 (10) (2002) 1648–1662. doi:10.1109/TAC.2002.803532.

[16] K. LARSSON, Investigation of a wave energy converter with a flywheel and a corresponding generator design, Master's thesis, CHALMERS UNIVERSITY OF TECHNOLOGY, Sweden (2012).

[17] M. Liu, R. Lin, S. Zhou, Y. Yu, A. Ishida, M. McGrath, B. Kennedy, M. Hajj, L. Zuo, Design, simulation and experiment of a novel high efficiency energy harvesting paver, Applied Energy 212 (2018) 966 – 975. doi:https://doi.org/10.1016/j.apenergy.2017.12.123.

[18] M. Bergmann, G. Bracco, F. Gallizio, E. Giorcelli, A. Iollo, G. Mattiazzo, M. Ponzetta, A two-way coupling cfd method to simulate the dynamics of a wave energy converter, in: OCEANS 2015 - Genova, 2015, pp. 1–6. doi:10.1109/OCEANS-Genova.2015.7271481.

[19] Y. Sang, H. Bora Karayaka, Yanjun Yan, J. Z. Zhang, E. Muljadi, Yi-Hsiang Yu, Energy extraction from a slider-crank wave energy converter under irregular wave conditions, in: OCEANS 2015 - MTS/IEEE Washington, 2015, pp. 1–7. doi:10.23919/OCEANS.2015.7401873.

[20] C. Liang, J. Ai, L. Zuo, Design, fabrication, simulation and testing of an ocean wave energy converter with mechanical motion rectifier, Ocean Engineering 136 (2017) 190 – 200. doi:https://doi.org/10.1016/j.oceaneng.2017.03.024.

[21] K. Ikago, K. Saito, N. Inoue, Seismic control of single-degree-of-freedom structure using tuned viscous mass damper, Earthquake Engineering & Structural Dynamics 41 (3) (2012) 453–474. doi:10.1002/eqe.1138.

[22] T. Asai, Y. Araki, K. Ikago, Energy harvesting potential of tuned inertial mass electromagnetic transducers, Mechanical Systems and Signal Processing 84, Part A (2017) 659 – 672. doi:10.1016/j.ymssp.2016.07.048.

[23] K. Sugiura, Y. Watanabe, T. Asai, Y. Araki, K. Ikago, Experimental characterization and performance improvement evaluation of an electromagnetic transducer utilizing a tuned inerter, Journal of Vibration and Control 26 (1-2) (2020) 56–72. doi:10.1177/1077546319876396.

[24] T. Asai, Y. Watanabe, Outrigger tuned inertial mass electromagnetic transducers for high-rise buildings subject to long period earthquakes, Engineering Structures 153 (2017) 404 – 410. doi:10.1016/j.engstruct.2017.10.040.

[25] T. Asai, Y. Araki, K. Ikago, Structural control with tuned inertial mass electromagnetic transducers, Structural Control and Health Monitoring 25 (2) (2018) e2059. doi:10.1002/stc.2059.

[26] J. Scruggs, S. Lattanzio, A. Taflanidis, I. Cassidy, Optimal causal control of a wave energy converter in a random sea, Applied Ocean Research 42 (2013) 1 – 15. doi:https://doi.org/10.1016/j.apor.2013.03.004.

[27] I. Cassidy, J. Scruggs, S. Behrens, H. P. Gavin, Design and experimental characterization of an electromagnetic transducer for large-scale vibratory energy harvesting applications, Journal of Intelligent Material Systems and Structures 22 (17) (2011) 2009–2024. doi:10.1177/1045389X11421824.

[28] Yaskawa electric corporation, `http://www.yaskawa.co.jp/en/`, Fukuoka, Japan (2019).

[29] R. Bansal, A Textbook of Fluid Mechanics and Hydraulic Machines, Laxmi Publications, 2005.

[30] R. Craig, A. Kurdila, Fundamentals of Structural Dynamics, Wiley, 2011.

[31] WAMIT, Inc., WAMIT, `http://www.wamit.com/index.htm`, MA, USA (2019).

[32] J. Scruggs, J. McCullagh, Analysis and design of vibratory energy harvesters employing three-phase ac transduction, Mechatronics 50 (2018) 104 – 120. doi:https://doi.org/10.1016/j.mechatronics.2018.01.015.

[33] Z. Yang, A. Copping, Marine Renewable Energy: Resource Characterization and Physical Effects, Springer International Publishing, 2017.

[34] T. H. Viuff, M. T. Andersen, M. Kramer, M. M. Jakobsen, Excitation forces on point absorbers exposed to high order non-linear waves, in: European Wave and Tidal Energy Conference, Aalborg, Denmark, 2013.

[35] E. Al Shami, R. Zhang, X. Wang, Point absorber wave energy harvesters: A review of recent developments, Energies 12 (1). doi:10.3390/en12010047.